Electrochemical Science Advances

Chemistry Europe
European Chemical Societies Publishing

SPECIAL ISSUE Bridging the Gap – Advancing Electrochemical Power-to-X Technologies towards Industrial Application

RESEARCH ARTICLE OPEN ACCESS

Thin Nickel Coatings on Stainless Steel for Enhanced Oxygen Evolution and Reduced Iron Leaching in Alkaline Water Electrolysis

Yashwardhan Deo[1] | Niklas Thissen[1] | Vera Seidl[1] | Julia Gallenberger[2] | Julia Hoffmann[3] | Jan P. Hofmann[2] | Bastian J. M. Etzold[3] | Anna K. Mechler[1]

[1]Electrochemical Reaction Engineering (AVT.ERT), RWTH Aachen University, Aachen, Germany | [2]Surface Science Laboratory, Department of Materials and Geosciences, Technical University of Darmstadt, Darmstadt, Germany | [3]Power-To-X Technologies, Friedrich-Alexander-Universität Erlangen-Nürnberg, Fürth, Germany

Correspondence: Yashwardhan Deo (yashwardhan.deo@avt.rwth-aachen.de) | Anna K. Mechler (anna.mechler@avt.rwth-aachen.de)

Received: 1 August 2024 | **Revised:** 30 October 2024 | **Accepted:** 17 November 2024

Funding: The financial support for this work was provided by the German Federal Ministry of Education and Research in the project "Prometh$_2$eus" (03HY105A, 03HY105H, 03HY105I, and 03HY105N).

Keywords: alkaline water electrolysis | electrodeposition | Fe leaching | oxygen evolution reaction | stainless steel

ABSTRACT

One of the most mature technologies for green hydrogen production is alkaline water electrolysis. However, this process is kinetically limited by the sluggish oxygen evolution reaction (OER). Improving the OER kinetics requires electrocatalysts, which can offer superior catalytic activity and stability in alkaline environments. Stainless steel (SS) has been reported as a cost-effective and promising OER electrode due to its ability to form active Ni-Fe oxyhydroxides during OER. However, it is limited by a high Fe-to-Ni ratio, leading to severe Fe-leaching in alkaline environments. This affects not only the electrode activity and stability but can also be detrimental to the electrolyzer system. Therefore, we investigate the effect of different Ni-coatings on both pure Ni- and SS-supports on the OER activity, while monitoring the extent of Fe-leaching during continuous operation. We show that thin layers of Ni enable enhanced OER activities compared to thicker ones. Especially, a less than 1 µm thick Ni layer on an SS-support shows superior OER activity and stability with respect to the bare supports. X-ray photoelectron spectroscopy reveals traces of oxidized Fe species on the catalyst surface after OER, suggesting that Fe from the SS may be incorporated into the layer during operation, forming active Ni-Fe oxyhydroxides with a very low Fe leaching rate. Utilizing inductively coupled plasma-optical emission spectroscopy, we prove that thin Ni layers on SS decrease Fe leaching whereas the Fe from the uncoated SS-support dissolves into the electrolyte during operation. Thus, OER active and stable electrodes can be obtained while maintaining a low Fe concentration in the electrolyte. This is particularly relevant for application in high-performance electrolyzer systems.

1 | Introduction

In recent years, alkaline water electrolysis (AWE) has gained significant importance as a technology for producing green hydrogen owing to its relatively low cost by using non-noble metals as catalysts, and its ability to be powered by renewable sources, such as solar or wind energy [1–4]. While this technology has already been commercially established, a major challenge of AWE is the improvement of the kinetically limited oxygen evolution reaction (OER), for which the development of suitable electrocatalysts is crucial. First-row transition metals, especially Ni-based materials, are promising candidates for OER catalysis

due to their low cost, high catalytic activity, earth abundance, and stability in alkaline media. In particular, the Ni-Fe system is of considerable importance in the field of AWE. Several studies have reported crucial improvements in the OER activity of Ni-based catalysts in the presence of small amounts of Fe [5–8]. Stainless steel (SS), notably, has gained considerable interest in recent years as an OER electrode. It is reported that the combination of Ni and Fe in SS can significantly activate the material by forming Ni-Fe oxyhydroxides under alkaline electrolysis conditions [9–14]. Furthermore, SS is cheap and readily available, thus, making it an attractive option for commercial alkaline electrolyzers.

However, SS itself may not provide the best OER activity because of its high Fe-to-Ni ratio. According to Klaus et al. [5] and Friebel et al. [15], a Fe content of 10–25 wt% in a Ni-Fe system provides optimal OER performance for Ni-Fe alloys. The Fe content in SS, indeed, is at least 50 wt%, irrespective of its purity grade. Another major drawback of SS is its poor stability in alkaline environments due to successive Fe, Cr, and Mn leaching, which makes it difficult to implement directly in commercial alkaline electrolyzers [9]. It is, therefore, necessary to modify SS, particularly with respect to its surface composition, to achieve a suitable electrode for water electrolysis. Various techniques have been reported to activate SS towards OER, for instance by chemical or electrochemical corrosion and oxidation of the SS surface [12, 14, 16–25]. The improvement in the OER performance using these modification techniques has been attributed to an increase in surface area [16, 18–20], surface enrichment of Ni [17, 21, 23, 26], and formation of active oxyhydroxides of Ni and Fe [14, 21, 23, 24]. While such modifications improve the OER performance of SS, it is important to note that they would, in most cases, not prevent Fe and Cr leaching during operation [9, 27], which could have major impacts on the electrolyzer system. Although Fe in the electrolyte is reported to have a positive effect on catalytic activity [5, 28–30], de Groot [31] mentioned that continuous Fe leaching is a challenge for operating high-performing electrolyzers that are less tolerant to Fe-impurities in the electrolyte. The negative effect of these Fe-impurities was ascribed to Fe deposition on noble metal cathodes, reducing their activity toward hydrogen evolution. While the rate of Fe dissolution may decrease over time as the SS surface is enriched with Ni [9], high Fe concentrations in the electrolyte would still be unavoidable, if surface activation is done in situ. On the other hand, Cr is reported to leach out as the toxic Cr^{6+} species [9, 32], which could cause environmental problems, even if the activation is done ex situ.

An alternative activation technique for SS is the deposition of active layers on its surface. Some recent studies have reported that the deposition of Ni-based layers activates SS toward OER [13, 33–38]. Wang et al. [34] and Perez-Alonso et al. [35] reported that Ni-Fe alloys deposited on SS support show improved activity due to the formation of active Ni-Fe oxyhydroxides. However, since the deposited layers were relatively thick (3–5 μm), the contribution of the SS support toward OER activity was not completely understood. Balram et al. [38] hypothesized that $Ni(OH)_2$ layers deposited on SS supports show enhanced OER activities owing to Fe^{3+} incorporation from the support in the NiOOH structure. The authors argued that "substrate-catalyst interactions" are important parameters that determine the catalytic activity, especially when the deposited layers are not too thick. Alhakemy et al. [37] reported that the activity of NiP-coated SS electrodes reaches an optimum for a certain deposition time, whereas higher deposition times do not provide additional improvement in activity. The authors attributed this behavior to a higher amount of surface cracks for low deposition times, which allow hydroxide species to diffuse through the layers and facilitate the Ni^{2+} to Ni^{3+} conversion. In contrast to Balram et al. [38], however, the authors did not mention any Fe effect from the SS support.

A critical, yet less discussed aspect of Ni-based layers deposited on SS is their ability to protect the support from dissolution. While the dissolution behavior of SS itself under AWE conditions has been extensively investigated [9, 21, 25, 27], there have been only a few studies that examine the dissolution behavior of SS-supported layers. Moranchell et al. [32] examined the Fe and Cr leaching behavior for SS electrodes modified with electrodeposited Ni layers under alkaline electrolysis conditions. The authors reported that such electrodes show reduced Fe and Cr leaching compared to bare SS due to the high alkaline stability of Ni. Nevertheless, the combined effect of the layer thickness on the activity and stability of the SS support is yet to be investigated in detail.

It is apparent that SS electrodes modified with Ni-based layers are interesting anode materials for OER, as they could have the dual advantage of improved catalytic activity and reduced dissolution of the support. In this study, we investigate electrodeposited Ni layers on SS plates (AISI 304) under alkaline electrolysis conditions. Electrodeposition is chosen as the synthesis technique because of its easy scalability as well as superior process control, especially with respect to layer thickness. As a reference, Ni layers with similar thicknesses are also deposited on pure Ni plates. The deposits are characterized using scanning electron microscopy (SEM) and energy-dispersive X-ray spectroscopy (EDX). We further investigate the electrochemical OER performance of the deposits in an in-house designed beaker cell using cyclic voltammetry (CV) and chronopotentiometry (CP). Finally, our results are substantiated by X-ray photoelectron spectroscopy (XPS) measurements, which aim to reveal changes in the surface composition of selected catalysts after the OER experiments. In addition, inductively coupled plasma-optical emission spectroscopy (ICP-OES) measurements are performed to track the Fe content in the electrolyte during OER experiments.

2 | Results and Discussion

2.1 | Characterization of the Deposited Layers

For a constant deposition current density, the deposit mass loading is expected to increase with the deposition time. The support material should ideally not impact the mass loading, but different supports may hinder or promote the competing hydrogen evolution reaction differently, which could change the Faradaic efficiency (FE) for the deposition. We therefore quantify the mass loadings obtained for our layers by weighing the SS and Ni plates before and after deposition and calculating the difference. For both supports a deposition time of 15 s led to a mass loading of 0.18 ± 0.03 mg/cm^2 while the 300 s deposits had a mass loading of 4.46 ± 0.03 mg/cm^2 (Figure S3).

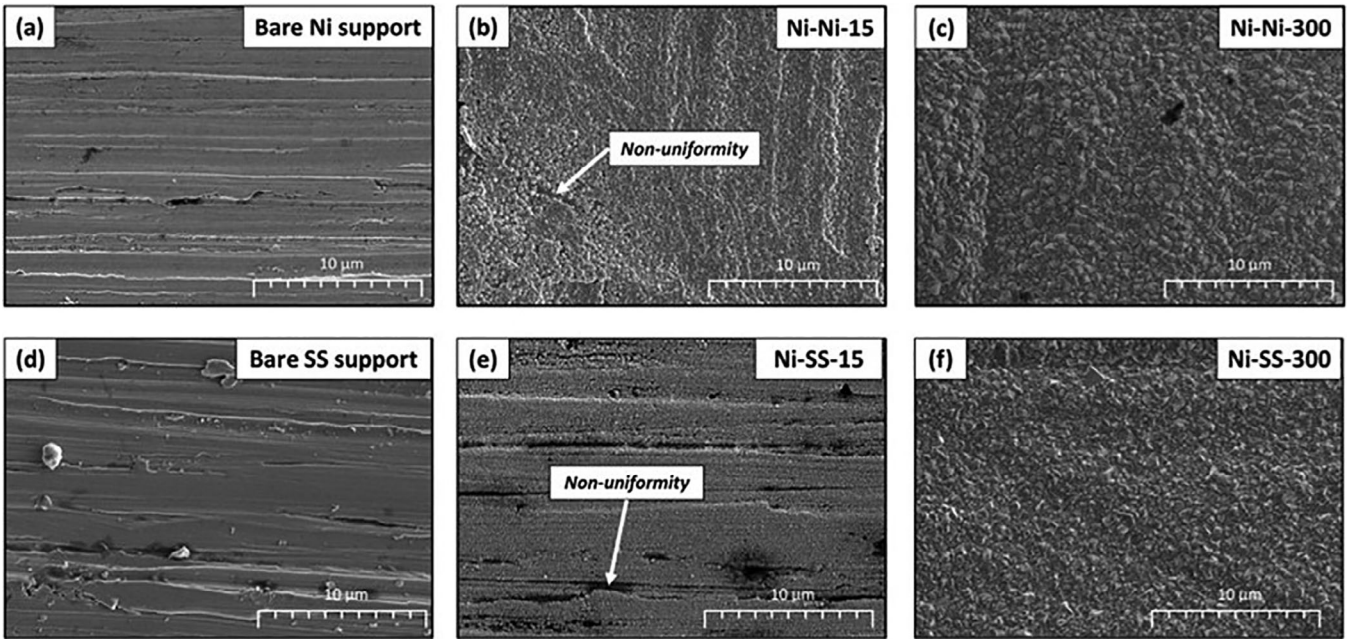

FIGURE 1 | Scanning electron microscopy (SEM) images taken in the secondary electron (SE) mode at 5000x magnification showing the surface morphology and homogeneity of the (a) bare Ni support, (b) Ni-Ni-15, and (c) Ni-Ni-300 deposits, as well as the (d) bare stainless steel (SS) support, (e) Ni-SS-15, and (f) Ni-SS-300 deposits.

The obtained mass values correspond to FEs of 81.5 ± 7.5% for the 15 s and 97.8 ± 0.3% for the 300 s deposits. The FE of the 15 s deposits is lower and less reproducible than that of the 300 s deposits, due to a higher relative error of the measured masses for the 15 s deposits. The average coating thicknesses of the layers were estimated by dividing the deposit mass loading by the density of pure Ni (8.9 g/cm^3), which resulted in layers of 0.2–0.3 µm for the 15 s and 4–5 µm for the 300 s deposits.

SEM analysis was carried out to observe the influence of the support and deposition time on the morphology, homogeneity, and composition of the resulting deposits. Figure 1a–f shows the SEM images for the bare Ni and SS supports and the subsequent electrodeposited Ni layers. As seen in Figure 1a,d, both Ni and SS bare supports were not mirror-polished, and the regular stripes by the preparation of the material are well visible. Figure 1b,e shows the microstructure of the Ni-Ni-15 and Ni-SS-15 deposits, respectively. A deposition time of 15 s does not allow sufficient time for the deposited grains to coarsen, and hence, in both cases, a fine-grained morphology can be observed. The pattern of the support roughness is also clearly seen in the microstructure due to the low coating thickness of the deposit. In Figure 1b, the stripes are vertical instead of horizontal, as the Ni-Ni-15 sample was placed in a rotated orientation in the microscope chamber. Moreover, the deposited layers from both Ni-Ni-15 and Ni-SS-15 are non-uniform, with some uncoated areas, indicating that the deposition time of 15 s may not have been sufficient to enable complete surface coverage. The uncoated areas are more clearly defined across the stripes of the support in the case of Ni-SS-15, suggesting that the low deposition time might have caused more deposition on the easily accessible protruding parts of the surface and less on the recessed parts. In contrast, the Ni-Ni-300 and Ni-SS-300 deposits, as shown in Figure 1c,f, respectively, are much more uniform. The support roughness pattern is also partially visible as vertical stripes for Ni-Ni-300 and horizontal stripes for Ni-SS-300 but is significantly less prominent due to the thicker deposit. Moreover, the longer deposition time has allowed for the development of a typical coarse-grained pyramidal microstructure of electrodeposited Ni [39].

The uniformity of the Ni-SS layers can be better visualized with the Ni and Fe EDX maps for the Ni-SS-15 and Ni-SS-300 deposits shown in Figure 2. The presence of Fe from the SS support is clearly visible for the uncoated parts of the Ni-SS-15 deposit. In contrast, Ni and Fe in the Ni-SS-300 deposit are uniformly distributed, indicating more uniform coverage of the Ni layer on the SS support.

2.2 | Electrochemical Testing and OER Activities

The electrocatalytic activity of the different layers was analyzed by CV as well as CP at 100 mA/cm^2 for 2 h in 1 M KOH at room temperature. Details on the experimental procedure can be found in the materials and methods section. Figure 3 shows the variation of the OER potentials required to reach 100 mA/cm^2 (E_{100}) in the CVs. Comparing E_{100} of the bare supports shows only little differences with potentials varying between 1.62 and 1.63 V. However, with a 15 s Ni deposition, there is a striking difference in the potentials of the two deposits, Ni-SS-15 and Ni-Ni-15. Ni-Ni-15 has a potential close to the bare Ni support, but Ni-SS-15 shows a significant potential drop of about 70 mV. As seen in the previous section, the morphology of these layers does not significantly depend on the support, which indicates that the support material itself has a considerable effect on the OER activity of the catalysts. As the Ni-SS-15 layer is inhomogeneous, the support material could be exposed to the electrolyte during the CV experiment, thus making it a Ni-rich Ni-Fe system. In contrast, the bare Ni

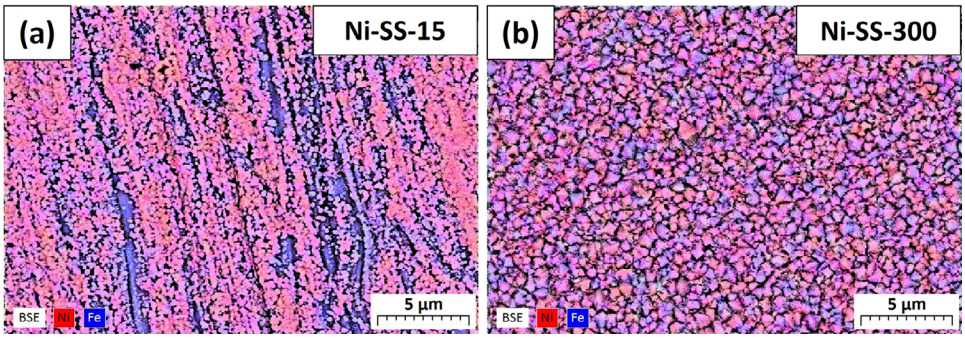

FIGURE 2 | Mixed energy-dispersive X-ray spectroscopy (EDX) elemental maps of Ni (red) and Fe (blue) taken in the backscattered electron (BSE) mode at 5000x magnification showing the distribution of the Ni layer on the stainless steel (SS) support for (a) Ni-SS-15 and (b) Ni-SS-300 deposits respectively.

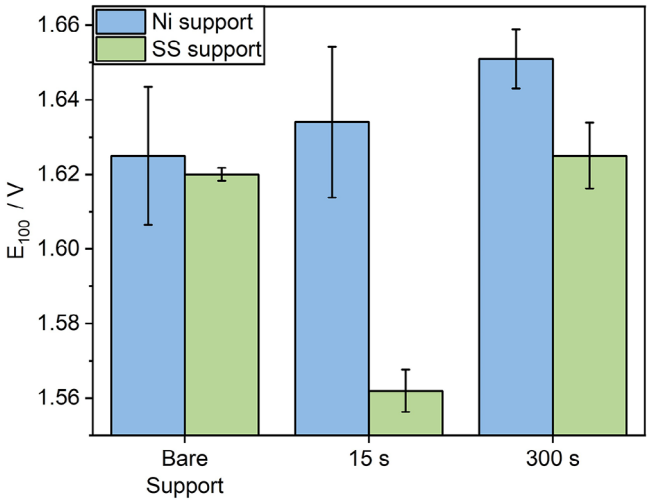

FIGURE 3 | iR-corrected oxygen evolution reaction (OER) potentials versus reversible hydrogen electrode (RHE) at 100 mA/cm^2 (E_{100}) for bare Ni and stainless steel (SS) support (left), and Ni (blue) and SS (green) supported layers for 15 s and 300 s deposition times. The potentials were obtained from cyclic voltammetry (CV) measurements and the error bars indicate the standard deviation obtained over three different measurements.

support might be too Fe-lean, and the bare SS support might be too Fe-rich to achieve an OER potential similar to Ni-SS-15. This is further discussed in the following section.

The layers deposited at 300 s deposition time show potentials similar to the bare supports, or even higher, indicating that a longer deposition time is rather detrimental to the catalyst activity. Especially, for the Ni-Ni deposits the potentials are higher than the bare support and increase with the deposition time. This may be due to the presence of impurities in the 99.2 wt% Ni support, which could positively affect the catalytic activity. The effect of these impurities would get reduced as thicker Ni layers are deposited on the support. Furthermore, the bare support is not polished and has stripes on its surface, as seen in Figure 1a. The deposited layers fill up these stripes (Figure 1b,c), which might lead to a reduced surface area, and therefore, lower OER activities.

Ni-SS-300 exhibits an OER potential of about 60 mV higher than Ni-SS-15. The high thickness and uniformity of the Ni layer in Ni-SS-300 results in a lower impact of the SS support than for the Ni-SS-15. Nevertheless, Ni-SS-300 still shows a potential of about 25 mV lower than Ni-Ni-300, indicating that the SS support could influence the catalytic activity, even for a uniform 4–5 µm Ni deposit.

Interestingly, the error bars, representing the standard deviation of three repetitive measurements, are significantly smaller for the SS-supported layers than for the Ni-supported layers. A possible explanation might be the effect of Fe present in the SS support, which stabilizes Ni oxyhydroxide species [40, 41]. These stable oxyhydroxides, most likely formed during the conditioning process, could give rise to more reproducible measurements for the SS support and, by extension, the Ni-SS deposits.

Figure 4a,b shows the change in E_{100} over a span of 2 h. The CP graphs of the Ni support as well as Ni-Ni-15 and Ni-Ni-300 (Figure 4a) show a similar trend. A significant decrease in potential can be observed in the first 0.5 h, most likely due to oxide formation. After 2 h the potential decrease slows down to an almost stable potential. It is interesting to note that, initially, the potentials of the bare Ni support and Ni-Ni-15 are almost in the same range (1.62–1.64 V), but the potential of the bare Ni support decreases more with time. At the end of 2 h, it reaches a potential of about 1.6 V, while the Ni-Ni-15 reaches a potential of about 1.63 V. Note that the bare support was naturally exposed to air before the OER studies for longer times compared to the deposited samples. To remove any originated surface oxides, the uncoated support was consequently treated with 10% aqueous HCl before the OER measurements. This should ensure equal original conditions for both bare support and deposited samples as the degree of surface oxidation is known to affect the OER activity. However, the acid treatment might have caused a roughening of the surface, making it more prone to re-oxidation with time, which could be the reason for its stronger activation. Comparing the Ni-Ni-15 and Ni-Ni-300 curves, the former seems to be more active. Nevertheless, the error range for both Ni-Ni-15 and Ni-Ni-300 curves has a significant overlap, and thus, the curves can be considered to be in a similar potential range. The Ni-Ni-15 CP curve, in particular, has a low reproducibility, which could be due to the non-uniformity of its deposited layer compared to the Ni-Ni-300 deposit.

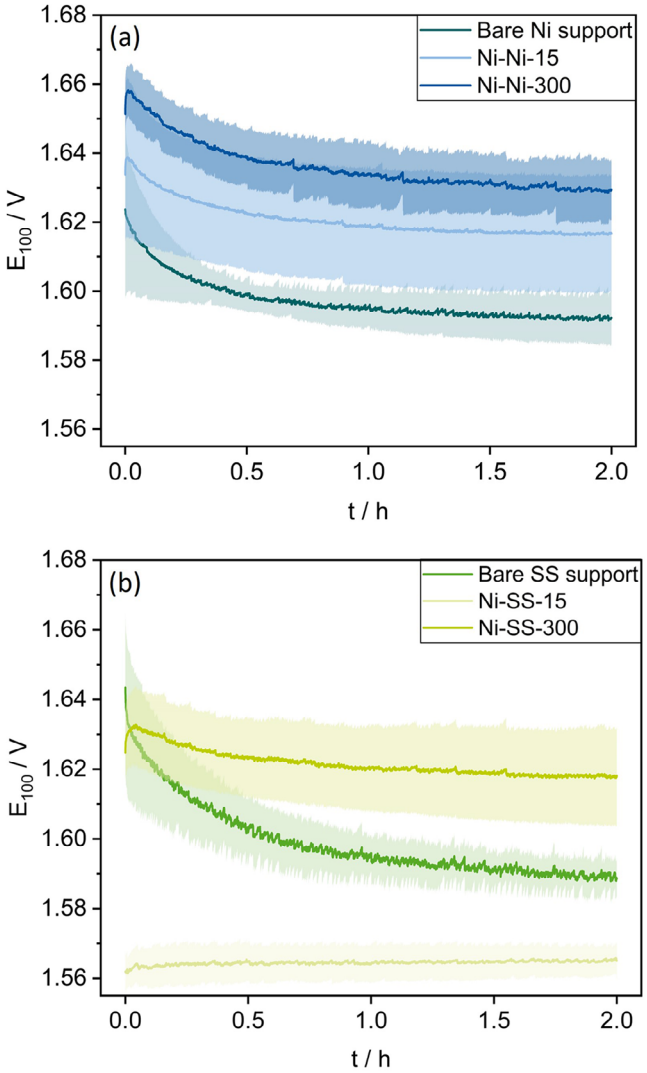

FIGURE 4 | Chronopotentiometric curves showing the variation of iR-corrected oxygen evolution reaction (OER) potentials versus reversible hydrogen electrode (RHE) at 100 mA/cm^2 (E_{100}) over a time of 2 h for (a) Ni support and Ni supported layers and (b) stainless steel (SS) support and SS supported layers. The standard deviations over three measurements are indicated by the shaded areas.

In contrast to those for Ni-Ni-15 and Ni-Ni-300, the CP curves for the bare SS support and SS supported layers (Figure 4b) show a different behavior. The potential of the Ni-SS-300 is initially at about 1.63 V and decreases down to 1.62 V after 2 h. This is slightly more active ($\Delta E \sim 20$ mV) compared to Ni-Ni-300 (Figure 4a) due to the beneficial effect of the SS support. This support effect is better observed in the CP measurement of Ni-SS-15. Its potential is initially about 1.56 V, which is lower than all other deposits in this study. There is no significant potential change over time, and the curve is reproducible within an error range of ±6 mV, indicating that the Ni-Fe oxyhydroxides species formed during the OER experiment (vide infra) may have an activating as well as a stabilizing effect on the catalyst.

Another important observation is the variation in potential with time in the case of the bare SS support. The potential significantly decreases from 1.64 V to 1.59 V ($\Delta E \sim 50$ mV). This might be

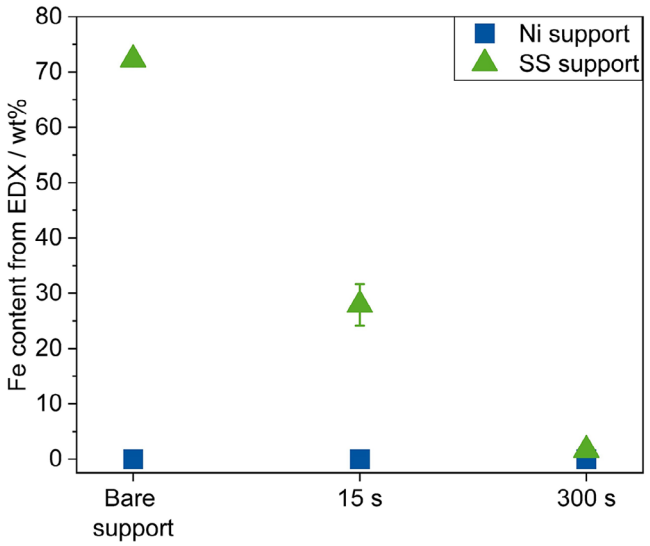

FIGURE 5 | Average Fe wt% detected by energy-dispersive X-ray spectroscopy (EDX) on the electrode surface for bare Ni and stainless steel (SS) supports as well as Ni- and SS-supported layers for 15 and 300 s deposition times. The error bars indicate the standard deviation obtained over two different measurements.

assigned to Fe dissolution from the SS in the electrolyte, which potentially increases the Ni-Fe ratio toward a more active surface composition. Additionally, a surface roughening effect is possible. The Fe-content in the samples pre- and post-electrochemistry as well as in the electrolyte is, hence, discussed further in the next section.

2.3 | The Impact of Fe

Since the OER activity of Ni catalysts is majorly affected by the presence of Fe, it is interesting to analyze the Fe content in the deposited layers [40]. Figure 5 shows the variation of the Fe content in the deposits with the deposition time for both Ni and SS-supported layers, as obtained from EDX measurements. For all Ni-supported layers, no Fe is detected by the EDX. This is reasonable considering the high purity of the support (99.2 wt%) and the absence of Fe in the deposition electrolyte. The bare SS support, in contrast, contains ~72 wt% Fe, which agrees with the AISI 304 SS composition (70–73 wt% Fe). Interestingly, Fe is also detected by EDX in the Ni-SS-15 and Ni-SS-300 samples. Approximately 25 wt% Fe is detected in the Ni-SS-15 deposit and 2 wt% in Ni-SS-300. One needs to keep in mind that an accelerating voltage of 15 kV for the EDX allows for electrons to penetrate the sample to a depth of approximately 1 µm [42]. Consequently, there is a considerable contribution of the Fe-rich support to the EDX signal for the Ni-SS-15 deposit, which has an estimated average coating thickness of about 0.2 µm. On the other hand, the Ni-SS-300 deposit has an estimated average coating thickness of 4–5 µm, which is significantly larger than the penetration depth of the EDX. This could mean that the Ni deposit is not completely uniform, or slightly porous, although this is not evident from the SEM images (Figure 1). Another possible explanation is the dissolution of Fe from the SS support in the deposition electrolyte, and co-deposition of this dissolved Fe with Ni, resulting in a Ni-Fe alloy deposit. However, this

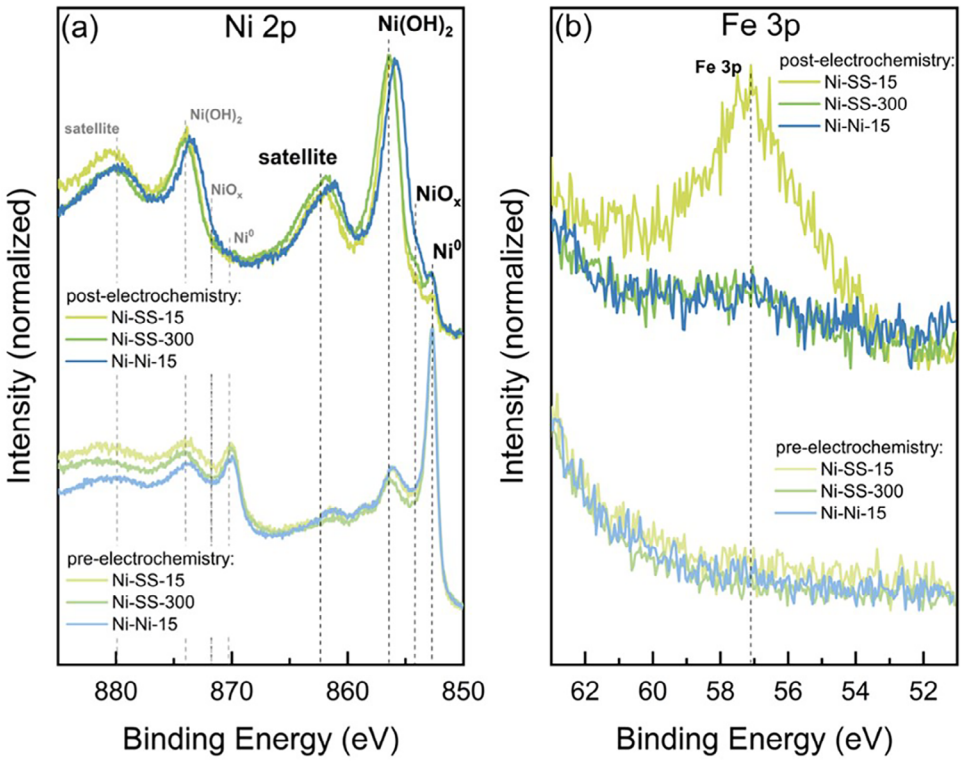

FIGURE 6 | (a) Ni 2p and (b) Fe 3p X-ray photoelectron spectroscopy (XPS) spectra for selected catalysts, Ni-SS-15 (light-green), Ni-SS-300 (dark green), and Ni-Ni-15 (blue), showing the change in catalyst surface composition from pre-electrochemistry (below) to post-electrochemistry (above).

cannot be entirely concluded from the EDX analysis alone, and hence, surface-sensitive analysis techniques are required for a more detailed understanding.

XPS measurements were performed for selected catalysts, that is, Ni-SS-15, Ni-SS-300, and Ni-Ni-15. The measurements were carried out both pre- and post-electrochemistry and the resulting Ni 2p and Fe 3p spectra were analyzed. The stronger Fe 2p core level peak was not analyzed due to its overlap with the dominant $L_3M_{23}M_{45}$ Auger line of Ni when using Al K_α X-ray radiation.

Figure 6a shows the pre-and post-electrochemistry Ni 2p XPS spectra for the catalysts. For the as-deposited samples, the Ni metal peak at a binding energy (BE) of 852.7 eV [43] is dominant for all catalysts, indicating that the surface predominantly contains Ni metal. A smaller peak at 856.3 eV corresponding to the presence of $Ni(OH)_2$ can also be observed [43]. This small amount of $Ni(OH)_2$ could have formed on the surface during the deposition or by exposure to air after the deposition. Post-electrochemistry, the intensity of the $Ni(OH)_2$ peak increases significantly, while the Ni metal peak is less intense, indicating the oxidation of the surface Ni metal to $Ni(OH)_2$. However, $Ni(OH)_2$ might not be the active phase formed during the OER process. According to Gallenberger et al. [44], an in-situ active NiOOH species may form during OER, but this phase is only stable at sufficiently high anodic potentials (>1.5 V), and decomposes to $Ni(OH)_2$ at lower potentials. The XPS measurements in this work were performed ex-situ, and the samples were taken out at OCP, which may be the reason why only the decomposed $Ni(OH)_2$ phase was detected.

Figure 6b shows the pre-and post-electrochemistry Fe 3p XPS spectra for the different electrodes. In the pre-electrochemistry spectra, Fe cannot be detected on any electrode surface, which is contrary to the EDX analysis. Since the analysis depth of XPS is much lower [45] as compared to EDX (~1 μm), it can be assumed that there is no Fe on the as-deposited catalyst surface. This also indicates that the Fe signal detected by the EDX likely came from the SS support and not from the catalyst surface. Post-electrochemistry, a Fe 3p peak at a BE of 57.1 eV can be seen, indicating the presence of oxidized Fe species, possibly FeOOH [43]. The intensity of this Fe 3p peak for the post-electrochemistry Ni-SS-300 and Ni-Ni-15 is significantly lower compared to Ni-SS-15. For Ni-SS-300 and Ni-Ni-15, this peak could arise due to the incorporation of Fe from the KOH. Nevertheless, the remarkably higher peak intensity for Ni-SS-15 indicates that Fe also originates from the SS support. It is important to note here, that for Fe-containing catalysts, a dynamic equilibrium is established under alkaline OER conditions due to simultaneous Fe-dissolution and Fe-redeposition [36, 46, 47]. Hoang et al. [36] hypothesized that the exposure of an SS-supported Ni catalyst to a KOH solution leads to the dissolution of Fe from the support and its redeposition on the Ni film, resulting in a Ni-Fe surface showing very high OER activities. This hypothesis would also be valid for the Ni-SS-15 catalyst reported herein, as the thin and non-uniform Ni coating would allow considerable Fe dissolution and redeposition, significantly increasing its catalytic activity.

In addition to the Fe in the support, the Fe in the electrolyte can also influence the catalyst's activity [5, 28, 40]. Moreover, changes in the Fe content in the electrolyte indicate the extent

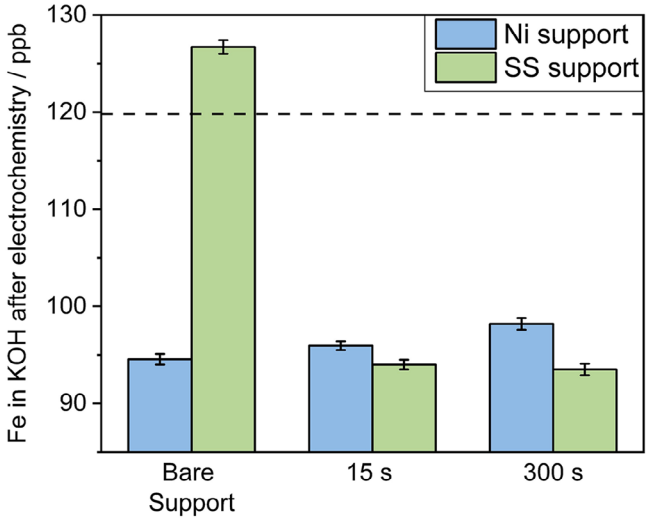

FIGURE 7 | Fe concentration in the KOH electrolyte obtained post electrochemistry for bare Ni and SS supports as well as Ni supported (blue) and SS supported (green) layers for 15 and 300 s deposition times. The pre-electrochemistry Fe concentration in the KOH electrolyte was constant for all experiments and is denoted by the dotted black line. The error bars represent the instrument error of the inductively coupled plasma-optical emission spectroscopy (ICP-OES).

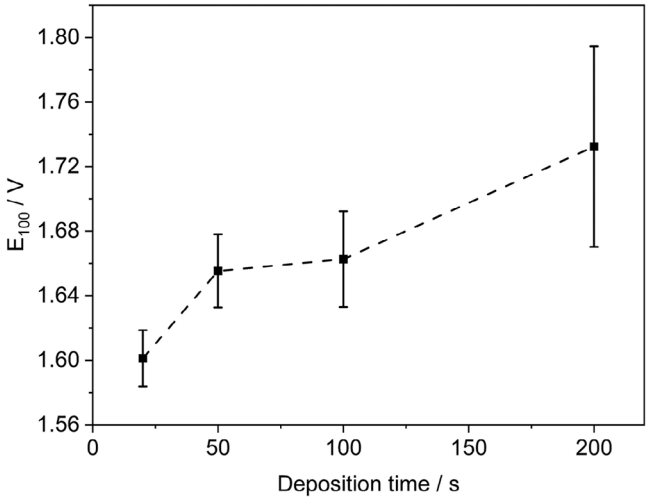

FIGURE 8 | iR-corrected oxygen evolution reaction (OER) potentials versus reversible hydrogen electrode (RHE) at 100 mA/cm^2 (E_{100}) for Ni layers deposited on stainless steel (SS) woven meshes at a constant current density of 50 mA/cm^2. The deposition time was varied from 20 to 200 s. The potentials were obtained from cyclic voltammetry (CV) measurements and the error bars indicate the standard deviation obtained over at least two different measurements.

of Fe leaching for SS-supported Ni layers. Here, ICP-OES was performed on freshly prepared KOH electrolyte as well as the KOH solution post-electrochemistry to observe any Fe dissolution or take-up during OER.

Figure 7 shows the variation of Fe concentration in KOH after the OER experiments for both Ni and SS-supported layers. The initial Fe concentration in the freshly prepared KOH is ca. 120 ppb, as denoted by the dotted line. For all samples except the bare SS support, the Fe concentration decreases by 20–25 ppb. This suggests that Fe is deposited from the electrolyte either on the anode, as detected by XPS for Ni-SS-15, Ni-SS-300, and Ni-Ni-15, or on the negatively charged cathode. The use of the bare SS sample, however, led to an increase in Fe concentration in the electrolyte to ca. 127 ppb, which indicates that Fe dissolution occurs from the bare SS support. While a total increase of 7 ppb seems to be small, the simultaneous deposition of Fe, present in the KOH, onto the anode or the cathode will also decrease the Fe content in the electrolyte, possibly resulting in an equilibrium concentration. Nevertheless, this observed Fe dissolution correlates well with the decrease in the OER potential observed in Figure 4b, suggesting that the dissolved Fe could be responsible for the increase in OER activity over time. It is also interesting to note that Ni-SS-15 resulted in similar low Fe contents in KOH as the other electrodes, indicating that a thin Ni layer is as effective in protecting Fe leaching from the support as a thick Ni layer. Hence, even if some Fe is dissolved, it is less than what is taken up, which ultimately results in a net decrease of Fe concentration in the KOH. It is likely that the rate of Fe dissolution is so low that the Fe released from the SS support is directly incorporated into the Ni-layer and hence not detected in the electrolyte after electrochemistry. This can also be validated by the strong Fe 3p peak observed in the Ni-SS-15 post-electrochemistry XPS spectra (Figure 6b), which indicates the presence of Fe on the deposit surface.

2.4 | Transferability of Results to SS Woven Meshes

As concluded in previous sections, thin Ni layers on SS plate supports show higher activity toward OER than thicker ones. In order to verify that these observations hold true for different support geometries and Ni deposition electrolytes, Ni layers were deposited on SS woven meshes with a projected area of 1 cm^2 using a commercial galvanic deposition bath from Umicore Galvanotechnik GmbH (NiRUNA 808). The deposition was carried out at a constant current density of 50 mA/cm^2 and the deposition time was varied from 20 to 200 s. These meshes were subsequently tested for their OER performance in 1 M KOH at 22°C using another in-house developed beaker cell. Details about the setup and experimental parameters for both Ni deposition and subsequent OER experiments can be found in the supplementary information.

Figure 8 shows the variation of E_{100} with the deposition time for the Ni-deposited SS woven meshes. E_{100} increases with the deposition time, which implies that similar to the plates, the SS meshes also show less activity with thicker Ni layers. Furthermore, increasing error bars with increasing deposition time can be observed, which is also similar to what is obtained for the SS plates (Figure 3). This reinforces the argument that stable Ni-Fe oxyhydroxide species are formed more easily with thinner Ni layers, and thus, show higher activity as well as better reproducibility during OER measurements. Despite the differences in the absolute E_{100} values for both woven meshes and plate support, resulting from several factors, such as deposit uniformity, layer thickness, and differences in experimental setups, a clear trend of increasing E_{100} values with the layer thickness can be observed, irrespective of the support geometry and the electrolyte used for deposition.

3 | Conclusion

In this work, Ni layers were electrodeposited on SS and Ni supports with varying loadings to understand the support and layer thickness contribution toward their electrochemical OER performance. A low deposition time resulted in non-uniform coatings and finer-grained morphologies, while a higher deposition time gave rise to uniform coarse-grained coatings. A thin Ni layer deposited with a deposition time of 15 s (Ni-SS-15) exhibited a noticeably higher OER activity than bare SS, whereas the activity decreased with thicker Ni layers. Similarly, Ni layers deposited on Ni supports exhibited significantly lower activities, indicating a favorable contribution of the SS support. The bare SS support itself exhibited a relatively high initial OER potential but was strongly activated over time. In contrast, Ni-SS-15 maintained a constant low potential, even below the final potential of the bare SS. The reason for this was attributed to the presence of an oxidized Fe-species, as revealed by XPS measurements, suggesting the formation of active Ni-Fe oxyhydroxides during OER. ICP-OES measurements of the electrolyte before and after the electrochemical procedure prove that Fe is dissolved in the KOH from the bare SS support. For all other electrodes studied, including Ni-SS-15, the Fe-content in the electrolyte actually dropped after OER, indicating a deposition rather than a dissolution. In conclusion, we report that a thin Ni layer deposited on a SS support provides a dual benefit of increased OER activity along with lower Fe leaching from the SS support. Additional investigations reveal similar activity trends for electrodeposited Ni layers on industrially relevant electrode geometries using commercial electrolytes. The transfer toward industrially relevant conditions remains outstanding. Yet, these first insights are promising, as thin Ni-coatings can effectively prevent Fe-leaching from Fe-rich supports in oxygen-evolving electrodes.

4 | Materials and Methods

4.1 | Electrodeposition

4.1.1 | Electrolyte, Electrodes, and Experimental Setup

The electrolyte used was a Watts Ni electrolyte containing 300 g/L nickel sulfate hexahydrate ($NiSO_4 \cdot 6H_2O$), 45 g/L nickel chloride hexahydrate ($NiCl_2 \cdot 6H_2O$), and 45 g/L boric acid (H_3BO_3) [48]. All chemicals were obtained from Thermo Fisher Scientific with a purity of >98%. 200 mL of electrolyte was prepared by dissolving the salts in ultrapure water at 60°C. The electrodeposition was performed in an in-house developed 4-electrode beaker cell setup. Two 1 × 1 cm pure Ni plates (>99.2 wt% Ni, HMW Hauner) were used as anodes and were placed on both sides of the cathode. As supports, and hence as cathodes, a 1 × 1 cm AISI 304 SS plate or another Ni plate were used, respectively. The electrodes were contacted by an in-house 3D-printed electrode holder made of RGD_{525}–High-Temperature Material from Stratasys, with a 0.5 mm Ni wire at the back for electrical contact. A Hg/Hg_2SO_4 reference electrode was placed near the working electrode. The potential of the reference electrode measured in the Watts Ni electrolyte was 755 ± 5 mV versus the reversible hydrogen electrode (RHE). The design of the electrodeposition setup is provided in the supplementary information (Figure S1).

4.1.2 | Electrode Pretreatment

Before deposition, the cathode was dipped in 10% HCl for 5 min, to remove any impurities or oxide layers on the surface. After the acid treatment, the sample was rinsed with distilled water and immediately placed in the deposition setup to avoid the reformation of extensive surface oxides.

4.1.3 | Deposition Parameters

The galvanostatic deposition was carried out using a Gamry 1010E potentiostat. The electrolyte volume, current density, temperature, and stirring rate were fixed at 175 mL, 50 mA/cm^2, 60°C, and 300 rpm for all depositions. Two different deposition times of 15 and 300 s were used for the deposition of Ni on both SS and Ni supports, resulting in four deposits: Ni-SS-15, Ni-SS-300, Ni-Ni-15, and Ni-Ni-300. Each deposition was carried out thrice to ensure reproducibility.

4.2 | Electrochemical OER experiments

4.2.1 | Setup

For the electrochemical OER experiments, another 3-electrode beaker cell setup was used, which is a modified version of the beaker cell designed by Thissen et al. [49] The deposited layers were used as the anode, and a 1 cm^2 piece of a commercial Ni Fly-net activated NRG electrode from De Nora was employed as the cathode. The electrodes were attached using in-house designed electrode holders similar to those used for electrodeposition. A Hg/HgO reference electrode was placed near the lower part of the anode in an inclined orientation to prevent evolved gas bubbles from sticking to the reference electrode. This ensured relatively low potential fluctuations during the electrochemical characterization. 1 M KOH solution was used as an electrolyte, prepared by dissolving KOH pellets (purity >85%, Chemsolute) in ultrapure water. The experiments were performed at ambient temperature (22°C) without any electrolyte agitation.

4.2.2 | Protocol

A Gamry 1010E potentiostat was used for the OER experiments. The electrochemical protocol consisted of an initial CV from 0.5 to 1.6 V versus RHE at a scan rate of 500 mV/s for 150 cycles to enable the formation of active surface oxides, denoted as conditioning. In the next step, the OER activity was measured using CVs at a scan rate of 5 mV/s. Lastly, a CP measurement was performed at a constant current density of 100 mA/cm^2 (geometric area) for 2 h to observe the electrode performance over time. Potentiostatic electrochemical impedance spectroscopy (PEIS) was performed at the open circuit potential (OCP) before every CV and CP to obtain the uncompensated resistance R_u. This was used for the post-iR drop correction of the obtained CVs and CPs. A graphical representation of the electrochemical protocol can be found in the supplementary information (Figure S2). For all iR-corrected CVs and CPs, the potentials are reported with respect to the RHE. The iR-corrected potential with respect to the Hg/HgO

reference electrode ($E_{\text{iRcorr vs. } \frac{Hg}{HgO}}$) was converted to the RHE scale ($E_{\text{iRcorr vs. RHE}}$) via the Nernst equation (Equation (1)), which was finally reported for all experiments [50].

$$E_{\text{iRcorr vs. RHE}} = E_{\text{iRcorr vs. Hg/HgO}} + \frac{2.303RT}{F}\text{pH} + E^{real}_{Hg/HgO\ (1M\ KOH)} \tag{1}$$

The real potential of the Hg/HgO electrode in 1 M KOH at 22°C ($E^{real}_{Hg/HgO\ (1\ M\ KOH)}$) was calculated using Equation (2) [50].

$$E^{real}_{Hg/HgO\ (1\ M\ KOH)} = E^{0}_{Hg/HgO} - \frac{RT}{2F} ln \frac{a_{OH^-}{}^2}{a_{H_2O}} \tag{2}$$

The necessary parameters, such as the pH of 1 M KOH, a_{OH^-}, and a_{H_2O} at 22°C were calculated using the Excel spreadsheet tool by Hausmann et al. [51] and finally, Equation (3) was obtained.

$$E_{\text{iRcorr vs. RHE}} = E_{\text{iRcorr vs. Hg/HgO}} + 0.924\ \text{V} \tag{3}$$

4.3 | Deposit Characterization

4.3.1 | Faradaic Efficiency Calculation

The FE of the deposition process was calculated using Equation (4).

$$FE = \frac{m_{deposited}}{(I_{app} \times t \times M_{Ni})/(Z \times f)} \times 100\% \tag{4}$$

where $m_{deposited}$ is the deposit mass loading obtained experimentally, I_{app} is the applied current (0.1 A), t is the deposition time (15 or 300 s), M_{Ni} is the molar mass of Ni (58.7 g mol^{-1}), z is the number of electrons transferred (2), and F is the Faraday constant (96485 C/mol).

4.3.2 | SEM and EDX

A Hitachi Schottky SU5000 FESEM was used to study the microstructure of the deposited layers as well as the bare Ni and SS supports. Images were taken in the secondary electron (SE) mode at a magnification of 5000x and at an accelerating voltage of 5 kV. A Bruker EDX, coupled with the SEM, was used to obtain the elemental compositions of the deposits. The accelerating voltage of the electrons was changed to 15 kV for the EDX analysis.

4.3.3 | X-ray photoelectron spectroscopy

XPS measurements were done with a hemispherical energy analyzer from SPECS (PHOIBOS 150) as part of the DAISY-FUN ultra-high vacuum cluster tool using monochromatic Al K_α radiation ($h\nu$ = 1486.74 eV). The spectra were acquired in fixed analyzer transmission mode. The pass energy was 20 eV for the survey scan and 10 eV for the core level spectra. The step size was 0.3 and 0.05 eV, respectively. The binding energy calibration of the system was done using sputter-cleaned Au, Cu, and Ag, to an accuracy of 0.1 eV. Data analysis was performed with CasaXPS, version 2.3.22.22 [52]. All spectra were calibrated to the Fermi edge E_F = 0 eV for the valence band edge of Ni metal. Handbooks of monochromatic XPS spectra were used to identify the metal or metal oxide species from the peak positions [43, 53].

4.3.4 | ICP-optical emission spectroscopy

An Agilent 5800 VDV ICP-OES was used to measure the Fe concentration in the KOH before and after OER experiments. The instrument was initially calibrated using a standard addition method, wherein known amounts of a Fe standard solution were added to a reference 1 M KOH solution, and the resulting intensities from the ICP-OES were used to obtain a calibration curve. The Fe concentration in the experimental KOH electrolytes was then calculated based on these calibration curves.

Author Contributions

Yashwardhan Deo: conceptualization (equal), investigation (lead), methodology (lead), formal analysis (lead), validation (equal), visualization (lead), writing–original draft (lead), and writing–review and editing (equal). **Niklas Thissen:** methodology (supporting) and writing–review and editing (equal). **Vera Seidl:** project administration (supporting), resources (supporting), supervision (supporting), and writing–review and editing (equal). **Julia Gallenberger:** formal analysis (supporting), investigation (supporting), validation (equal), visualization (supporting), and writing–review and editing (equal). **Julia Hoffmann:** investigation (supporting), visualization (supporting), and writing–review and editing (equal). **Jan P. Hofmann:** conceptualization (equal), investigation (equal), methodology (supporting), formal analysis (supporting), validation (supporting), and writing–review and editing (equal). **Bastian J. M. Etzold:** conceptualization (supporting), funding acquisition (supporting), project administration (supporting), resources (supporting), supervision (supporting), and writing–review and editing (equal). **Anna K. Mechler:** conceptualization (equal), funding acquisition (lead), project administration (lead), resources (lead), supervision (lead), and writing–review and editing (equal).

Acknowledgments

The financial support for this work was provided by the German Federal Ministry of Education and Research (BMBF) under the project "PrometH_2eus" (FKZ 03HY105A, 03HY105H, 03HY105I, and 03HY105N). We thank our industry partner De Nora, particularly Dr. Praveen V. Narangoda, for continuous guidance and support. The Umicore Galvanotechnik GmbH, personally Dr. Artur Wiser and Dr. Christian Goerens, is acknowledged for providing SS woven meshes and electrodeposition baths. Finally, we would like to thank Ms. Malgorzata Kwiatkowska (AVT.ERT) and Ms. Karin Faensen (AVT.CVT), for conducting ICP-OES and SEM-EDX measurements, respectively.

Open access funding enabled and organized by Projekt DEAL.

Conflicts of Interest

The authors declare no conflicts of interest.

Data Availability Statement

The data that support the findings of this study are openly available in Zenodo at https://doi.org/10.5281/zenodo.13772144.

References

1. M. A. Khan, H. Zhao, W. Zou, et al., "Recent Progresses in Electrocatalysts for Water Electrolysis," *Electrochemical Energy Reviews* 1 (2018): 483–530.

2. M. I. Jamesh and X. Sun, "Recent Progress on Earth Abundant Electrocatalysts for Oxygen Evolution Reaction (OER) in Alkaline Medium to Achieve Efficient Water Splitting—A Review," *Journal of Power Sources* 400 (2018): 31–68.

3. Z. Angeles-Olvera, A. Crespo-Yapur, O. Rodríguez, J. L. Cholula-Díaz, L. M. Martínez, and M. Videa, "Nickel-Based Electrocatalysts for Water Electrolysis," *Energies* 15 (2022): 1609.

4. J. Brauns and T. Turek, "Alkaline Water Electrolysis Powered by Renewable Energy: A Review," *Processes* 8 (2020): 248.

5. S. Klaus, Y. Cai, M. W. Louie, L. Trotochaud, and A. T. Bell, "Effects of Fe Electrolyte Impurities on $Ni(OH)_2$/NiOOH Structure and Oxygen Evolution Activity," *Journal of Physical Chemistry C* 119 (2015): 7243–7254.

6. S. Klaus, M. W. Louie, L. Trotochaud, and A. T. Bell, "Role of Catalyst Preparation on the Electrocatalytic Activity of $Ni_{1-x}Fe_xOOH$ for the Oxygen Evolution Reaction," *Journal of Physical Chemistry C* 119 (2015): 18303.

7. M. W. Louie and A. T. Bell *Journal of the American Chemical Society* 5 (2013): 1.

8. M. Steimecke, G. Seiffarth, and M. Bron, "In Situ Characterization of Ni and Ni/Fe Thin Film Electrodes for Oxygen Evolution in Alkaline Media by a Raman-Coupled Scanning Electrochemical Microscope Setup," *Analytical Chemistry* 89 (2017): 10679.

9. N. Todoroki and T. Wadayama, "Dissolution of Constituent Elements From Various Austenitic Stainless Steel Oxygen Evolution Electrodes Under Potential Cycle Loadings," *International Journal of Hydrogen Energy* 47 (2022): 32753.

10. Z. Cheng, C. Qu, C. Gao, L. Kong, P. Yin, and J. Lin, "Promoting Surface Reconstruction of Low-Cost Stainless Steel Catalyst for Efficient Oxygen Evolution Reaction," *Chemistry: A European Journal* 29 (2023): e202300741.

11. J. Ekspong and T. Wågberg, "Stainless Steel as a Bi-Functional Electrocatalyst—A Top-Down Approach," *Materials* 12 (2019): 2128.

12. F. Moureaux, P. Stevens, G. Toussaint, and M. Chatenet, "Timely-Activated 316L Stainless Steel: A Low Cost, Durable and Active Electrode for Oxygen Evolution Reaction in Concentrated Alkaline Environments," *Applied Catalysis B: Environment* 258 (2019): 117963.

13. J. S. Chen, J. Ren, M. Shalom, T. Fellinger, and M. Antonietti, "Stainless Steel Mesh-Supported NiS Nanosheet Array as Highly Efficient Catalyst for Oxygen Evolution Reaction," *ACS Applied Materials & Interfaces* 8 (2016): 5509–5516.

14. D. Tang, O. Mabayoje, Y. Lai, Y. Liu, and C. B. Mullins, "In Situ Growth of Fe(Ni)OOH Catalyst on Stainless Steel for Water Oxidation," *ChemistrySelect* 2 (2017): 2230–2234.

15. D. Friebel, M. W. Louie, M. Bajdich, et al., "Identification of Highly Active Fe Sites in (Ni,Fe)OOH for Electrocatalytic Water Splitting," *Journal of the American Chemical Society* 137 (2015): 1305–1313.

16. M. J. Lavorante and J. I. Franco, "Performance of Stainless Steel 316L Electrodes With Modified Surface to be Use in Alkaline Water Electrolyzers," *International Journal of Hydrogen Energy* 41 (2016): 9731–9737.

17. S. Anantharaj, M. Venkatesh, A. S. Salunke, T. V. S. V. Simha, V. Prabu, and S. Kundu, "High-Performance Oxygen Evolution Anode From Stainless Steel via Controlled Surface Oxidation and Cr Removal," *ACS Sustainable Chemistry & Engineering* 5 (2017): 10072.

18. J. Shen, M. Wang, L. Zhao, P. Zhang, J. Jiang, and J. Liu, "Amorphous Ni(Fe)O H -Coated Nanocone Arrays Self-Supported on Stainless Steel Mesh as a Promising Oxygen-Evolving Anode for Large Scale Water Splitting," *Journal of Power Sources* 389 (2018): 160–168.

19. J. Shen, M. Wang, L. Zhao, J. Jiang, H. Liu, and J. Liu, "Self-Supported Stainless Steel Nanocone Array Coated With a Layer of Ni–Fe Oxides/(Oxy)Hydroxides as a Highly Active and Robust Electrode for Water Oxidation," *ACS Applied Materials & Interfaces* 10 (2018): 8786–8796.

20. F. Moureaux, P. Stevens, G. Toussaint, and M. Chatenet, "Development of an Oxygen-Evolution Electrode From 316L Stainless Steel: Application to the Oxygen Evolution Reaction in Aqueous Lithium–Air Batteries," *Journal of Power Sources* 229 (2013): 123–132.

21. H. Schäfer, S. Sadaf, L. Walder, et al., "Stainless Steel Made to Rust: A Robust Water-Splitting Catalyst With Benchmark Characteristics," *Energy & Environmental Science* 8 (2015): 2685–2697.

22. M. Chatenet, B. G. Pollet, D. R. Dekel, et al., "Water Electrolysis: From Textbook Knowledge to the Latest Scientific Strategies and Industrial Developments," *Chemical Society Reviews* 51 (2022): 4583–4762.

23. H. Schäfer, D. M. Chevrier, P. Zhang, et al., "Electro-Oxidation of Ni42 Steel: A Highly Active Bifunctional Electrocatalyst," *Advanced Functional Materials* 26 (2016): 6402–6417.

24. N. Todoroki and T. Wadayama, "Heterolayered Ni–Fe Hydroxide/Oxide Nanostructures Generated on a Stainless-Steel Substrate for Efficient Alkaline Water Splitting," *ACS Applied Materials & Interfaces* 11 (2019): 44161.

25. N. Todoroki, A. Shinomiya, and T. Wadayama, "Nanostructures and Oxygen Evolution Overpotentials of Surface Catalyst Layers Synthesized on Various Austenitic Stainless Steel Electrodes," *Electrocatalysis* 13 (2022): 116–125.

26. G. R. Zhang, L. L. Shen, P. Schmatz, K. Krois, and B. J. M. Etzold, "Cathodic Activated Stainless Steel Mesh as a Highly Active Electrocatalyst for the Oxygen Evolution Reaction With Self-Healing Possibility," *Journal of Energy Chemistry* 49 (2020): 153–160.

27. T. Nakagawa, H. Matsushima, M. Ueda, and H. Ito, "Corrosion Behavior of SUS 304L Steel in pH 13 NaOH Solution," *Electrochemistry* 88 (2020): 468–474.

28. I. Spanos, J. Masa, A. Zeradjanin, and R. Schlögl, "The Effect of Iron Impurities on Transition Metal Catalysts for the Oxygen Evolution Reaction in Alkaline Environment: Activity Mediators or Active Sites?" *Catalysis Letters* 151 (2021): 1843–1856.

29. L. Trotochaud, S. L. Young, J. K. Ranney, and S. W. Boettcher, "Nickel–Iron Oxyhydroxide Oxygen-Evolution Electrocatalysts: The Role of Intentional and Incidental Iron Incorporation," *Journal of the American Chemical Society* 136 (2014): 6744–6753.

30. S. Bhandari, P. V. Narangoda, S. O. Mogensen, M. F. Tesch, and A. K. Mechler, "Effect of Experimental Parameters on the Electrocatalytic Performance in Rotating Disc Electrode Measurements: Case Study of Oxygen Evolution on Ni–Co-Oxide in Alkaline Media," *ChemElectroChem* 9 (2022): e202200479.

31. M. T. de Groot, "Alkaline Water Electrolysis: With or Without Iron in the Electrolyte?" *Current Opinion in Chemical Engineering* 42 (2023): 100981.

32. F. A. Soriano Moranchell, J. M. Sandoval Pineda, J. N. Hernández Pérez, U. S. Silva-Rivera, C. A. Cortes Escobedo, and R. d. G. González Huerta, "Electrodes Modified With Ni Electrodeposition Decrease Hexavalent Chromium Generation in an Alkaline Electrolysis Process," *International Journal of Hydrogen Energy* 45 (2020): 13683.

33. Y. Gao, T. Xiong, Y. Li, Y. Huang, Y. Li, and M. S. J. T. Balogun, "A Simple and Scalable Approach To Remarkably Boost the Overall Water Splitting Activity of Stainless Steel Electrocatalysts," *ACS Omega* 4 (2019): 16130.

34. Y. Wang, N. Williamson, R. Dawson, and N. Bimbo, "Electrodeposition of Nickel–Iron on Stainless Steel as an Efficient Electrocatalyst Coating for the Oxygen Evolution Reaction in Alkaline Conditions," *Journal of Applied Electrochemistry* 53 (2023): 877–892.

35. F. J. Pérez-Alonso, C. Adán, S. Rojas, M. A. Peña, and J. L. G. Fierro, "Ni/Fe Electrodes Prepared by Electrodeposition Method Over Different Substrates for Oxygen Evolution Reaction in Alkaline Medium," *International Journal of Hydrogen Energy* 39 (2014): 5204–5212.

36. T. T. H. Hoang and A. A. Gewirth, "High Activity Oxygen Evolution Reaction Catalysts From Additive-Controlled Electrodeposited Ni and NiFe Films," *ACS Catalysis* 6 (2016): 1159–1164.

37. A. Z. Alhakemy, A. B. Ahmed Amine Nassr, A. E. H. Kashyout, and Z. Wen, "Modifying the 316L Stainless Steel Surface by an Electrodeposition Technique: Towards High-Performance Electrodes for Alkaline Water Electrolysis," *Sustainable Energy & Fuels* 6 (2022): 1382–1397.

38. A. Balram, H. Zhang, and S. Santhanagopalan, "Enhanced Oxygen Evolution Reaction Electrocatalysis via Electrodeposited Amorphous α-Phase Nickel-Cobalt Hydroxide Nanodendrite Forests," *ACS Applied Materials & Interfaces* 9 (2017): 28355.

39. A. Boukhouiete, S. Boumendjel, and N. E. H. Sobhi, "Effect of Current Density on the Microstructure and Morphology of the Electrodeposited Nickel Coatings," *Turkish Journal of Chemistry* 45 (2021): 1599–1608.

40. S. Anantharaj, S. Kundu, and S. Noda, ""The Fe Effect": A Review Unveiling the Critical Roles of Fe in Enhancing OER Activity of Ni and Co Based Catalysts," *Nano Energy* 80 (2021): 105514.

41. Y. J. Ye, N. Zhang, and X. X. Liu, "Amorphous NiFe(oxy)Hydroxide Nanosheet Integrated Partially Exfoliated Graphite Foil for High Efficiency Oxygen Evolution Reaction," *Journal of Materials Chemistry A* 5 (2017): 24208.

42. J. J. Friel, R. Terborg, S. Langner, T. Salge, B. N. GmbH, M. Rohde, and J. Berlin, "X-Ray and Image Analysis in Electron Microscopy," Pro Business (2017).

43. B. V. Crist, "Handbooks of Monochromatic XPS Spectra-Commercially Pure Binary Oxides," XPS International LLC (2005).

44. J. Gallenberger, H. Moreno Fernández, A. Alkemper, et al., "Stability and Decomposition Pathways of the NiOOH OER Active Phase of NiO_X Electrocatalysts at Open Circuit Potential Traced by Ex Situ and in Situ Spectroscopies," *Catalysis Science & Technology* 13 (2023): 4693–4700.

45. F. A. Stevie and C. L. Donley, "Introduction to X-Ray Photoelectron Spectroscopy," *Journal of Vacuum Science & Technology, A: Vacuum, Surfaces, and Films* 38 (2020): 063204.

46. N. Yu, J. Y. Lv, Z. C. Guo, et al., "Strong Lewis Acid-Induced Self-Healing of Loose FeOOH for Alkaline Oxygen Evolution," *Journal of Chemical Engineering* 487 (2024): 150253.

47. C. Gohlke, J. Gallenberger, N. Niederprüm, et al., "Boosting the Oxygen Evolution Reaction Performance of Ni-Fe-Electrodes by Tailored Conditioning," *ChemElectroChem* 11 (2024): 202400318.

48. G. A. Di Bari, "*Electrodeposition of Nickel," in Modern Electroplating*, eds. M. Schlesinger and M. Paunovic (New York: John Wiley & Sons, 2011), 79–114.

49. N. Thissen, J. Hoffmann, S. Tigges, et al., "Industrially Relevant Conditions in Lab-Scale Analysis for Alkaline Water Electrolysis," *ChemElectroChem* 11 (2023): e202300432.

50. K. Kawashima, R. A. Márquez, Y. J. Son, et al., "Accurate Potentials of Hg/HgO Electrodes: Practical Parameters for Reporting Alkaline Water Electrolysis Overpotentials," *ACS Catalysis* 13 (2023): 1893–1898.

51. J. N. Hausmann, B. Traynor, R. J. Myers, M. Driess, and P. W. Menezes, "The pH of Aqueous NaOH/KOH Solutions: A Critical and Non-Trivial Parameter for Electrocatalysis," *ACS Energy Letters* 6 (2021): 3567–3571.

52. N. Fairley, V. Fernandez, M. Richard-Plouet, et al., "Systematic and Collaborative Approach to Problem Solving Using X-Ray Photoelectron Spectroscopy," *Applications of Surface Science* 5 (2021): 100112.

53. B. V. Crist, "Handbook of Monochromatic XPS Spectra," XPS International LLC (1999).

Supporting Information

Additional supporting information can be found online in the Supporting Information section.